# Imaging ferroelastic domain walls in hybrid improper ferroelectric $Sr_3Sn_2O_7$

Ashley M. Sargent,[†] Kevin A. Smith,[†] Kai Du,[‡] Xianghan Xu,[‡] Sang-Wook Cheong,[‡] Stephanie N. Gilbert Corder,[¶] Hans A. Bechtel,[¶] and Janice L. Musfeldt*[,†,§]

†*Department of Chemistry, University of Tennessee, Knoxville, Tennessee, 37996, USA.*

‡*Keck Center for Quantum Magnetism and Department of Physics and Astronomy, Rutgers University, Piscataway, New Jersey 08854 USA*

¶*Advanced Light Source Division, Lawrence Berkeley National Laboratory, Berkeley, California 94720 USA*

§*Department of Physics and Astronomy, University of Tennessee, Knoxville, Tennessee, 37996, USA.*

E-mail: musfeldt@utk.edu

**Abstract**

We combined synchrotron-based near field infrared spectroscopy and atomic force microscopy to image the properties of ferroelastic domain walls in $Sr_3Sn_2O_7$. Although frequency shifts at the walls are near the limit of our sensitivity, we can confirm semiconducting rather than metallic character and widths between 20 and 60 nm. The latter is significantly narrower than in other hybrid improper ferroelectrics like $Ca_3Ti_2O_7$. We attribute this trend to the softer lattice in $Sr_3Sn_2O_7$ which may enable the octahedral tilt and rotation order parameters to evolve more quickly across the wall without significantly increased strain. These findings are crucial for the understanding of phononic

properties at interfaces and the development of domain wall-based devices.

**Keywords:** hybrid improper ferroelectrics, ferroelastic domain walls, symmetry analysis, near field infrared imaging

The discovery of hybrid improper ferroelecticity in layered perovksites has led to a number of new and exciting room temperature ferroelectrics, particularly in the $n = 2$ Ruddlesden-Popper $A_3B_2O_7$ family of materials.[1–8] The key feature of hybrid improper ferroelectricity is a trilinear coupling between the polarization and two other structural order parameters, which are typically rotations and tilts of the corner-connected network of metal oxide octahedra in the crystal structure [Fig. 1(a)]. $Ca_3Ti_2O_7$ was the first experimentally confirmed hybrid improper ferroelectric,[6] although other systems including $Sr_3Sn_2O_7$, $Sr_3Zr_2O_7$, and $Ca_3Mn_2O_7$ developed quickly by taking advantage of similar design principles.[9–13] These materials are very sensitive to chemical substitution. This responsiveness is beautifully illustrated by the fact that a plot of Curie temperature ($T_C$) vs. tolerance factor is linear for this family of materials.[11] Properties like the band gap are highly tunable as well,[14] and rare earth ions can be incorporated to yield light emission.[15] In terms of external stimuli, both temperature and pressure trigger the development of different structural phases,[10,16–18] some of which are predicted to display negative thermal expansion.[19–21] This family of materials is spatially heterogeneous with interfaces in the form of domain walls.[22] In $Ca_3Ti_2O_7$, these defects consist of linear ferroelastic walls and meandering ferroelectric walls with both vortices and antivortices.[6,23,24] Sr substitution on the $A$ site significantly increases domain wall density.[6,23] Recent infrared imaging of the ferroelastic walls in $Ca_3Ti_2O_7$ reveals both semiconducting character and exceptionally wide ferroelastic walls (between 60 and 160 nm) as shown in Fig. 1(e).[25] These findings are different from prior conducting atomic force microscopy as well as expectations for atomically thin walls, suggesting that residual structural distortions across twin boundaries in hybrid improper ferroelectrics merit additional investigation.[26–28] We therefore turn to $Sr_3Sn_2O_7$ to further explore the phononic properties of domain walls. In addition to being a rare instance of a Sn-based ferroelectric with switchable polarization,[9,13] the ferroelastic walls in this system are easy to visualize in a microscope using linearly polarized light as well as in the normal field of view of the near field setup

[Fig. 1(b,c)]. Atomic force microscopy also highlights topographically smooth twin boundaries [Fig. 1(d)] that are well-suited for near field line scans. This platform allows us to reexamine questions relevant to domain wall conductivity and width and, at the same time, begin to unravel structure-property relations in an unusual setting.

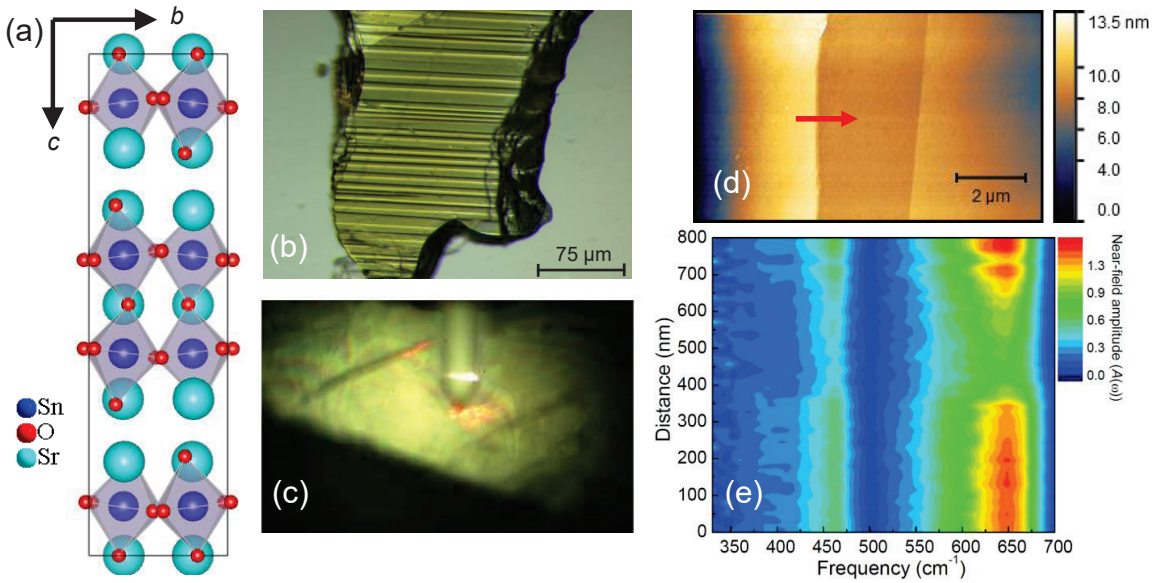


Figure 1: (a) Crystal structure of $Sr_3Sn_2O_7$ (space group $A2_1am$).[9] This $n$=2 Ruddlesden-Popper system has both perovskite and rock salt layers. (b) Photograph of the linear ferroelastic domain walls in a large single crystal of $Sr_3Sn_2O_7$ taken under linearly polarized light. The meandering ferroelectric domain walls are not visible in this image. (c) Image of the crystal surface and top of the cantilever tip along with two ferroelastic domain walls. (d) Atomic force microscope image of the surface of $Sr_3Sn_2O_7$, which is extremely flat. The red arrow shows how we carry out a typical near field line scan. The height is indicated. (e) Contour plot of the synchrotron-based near field infrared amplitude across a ferroelastic domain wall in $Ca_3Ti_2O_7$.[25] The wall in this image is approximately 160 nm wide as evidenced by changes in the Ti-O stretching and Ti-O-Ti bending modes near 650 and 450 $cm^{-1}$, respectively.

In order to further explore the phononic properties of twin boundary-type interfaces in hybrid improper ferroelectrics, we combined synchrotron-based near field nano-spectroscopy with atomic force microscopy to image the ferroelastic domain walls in $Sr_3Sn_2O_7$. We find that these walls have widths on the order of 40 nm and step sizes of only ≈7 nm, so the interface is narrow and relatively flat. They are also semiconducting, with reduced amplitude at the wall and no evidence for metallic character - in line with prior work on $Ca_3Ti_2O_7$.[25]

Despite these similarities, the ferroelastic domain walls in $Sr_3Sn_2O_7$ are significantly narrower than those in other hybrid improper ferroelectrics such as $Ca_3Ti_2O_7$ [Fig. 1(e)]. Analysis of the lattice constants, tolerance factor, and local structure reveals a softer lattice, suggesting that the octahedral tilt and rotational order parameters[8] rotate more quickly across the wall in $Sr_3Sn_2O_7$ compared to $Ca_3Ti_2O_7$. The ability to bring structure-property arguments to an entirely new setting is a significant conceptual advance revealing that the underlying mechanism of reduced domain wall width is indeed the soft lattice in $Sr_3Sn_2O_7$. In addition to understanding the fundamental aspects of these interfaces, real space imaging of ferroic materials is important for heat and strain management in domain wall-based logic and neuromorphic computing devices.

**Crystal growth and domain wall identification:** High quality single crystals of the hybrid improper ferroelectric $Sr_3Sn_2O_7$ were grown using laser floating zone techniques as described previously.[13] A stereo microscope equipped with a linear polarizer was used to locate ferroelastic walls, and atomic force microscopy (AFM) was employed to confirm cleanliness and to identify particular domain walls in candidate scan areas.

**Far field spectroscopy:** Traditional far infrared measurements were performed using a Bruker 113V Fourier transform spectrometer equipped with a series of beamsplitters and a helium-cooled bolometer detector covering the 22 - 690 $cm^{-1}$ range. Far field techniques are aperature-based, so they are limited by the diffraction limit of light - resulting in a spot size of a few microns.

**Synchrotron based near-field infrared spectroscopy:** Near-field infrared measurements were performed using the Advanced Light Source synchrotron at beamline 2.4 at Lawrence Berkeley National Laboratory.[29–34] Similar to a far field infrared set-up, the in-

frared light is guided using an asymmetric Michelson interferometer where one arm is a moving mirror and the other is an AFM (Neaspec neaSNOM). Infrared light from the synchrotron is focused on a standard conducting AFM tip which serves as an antennae. The tip is operated in a intermittent contact (tapping) mode with an oscillation amplitude of ≈80 nm when engaged and has a resonance frequency of between 240 and 380 kHz. As this is a tip-based technique, spatial resolution is tip-dependent and on the order of 20 × 20 $nm^2$. The scattered light from the tip is combined with reference light obtained from a moving parabolic mirror on a beamsplitter and detected by a liquid-helium cooled Ge:Cu detector equipped with low noise components. The interferogram is Fourier transformed providing both amplitude and phase information which corresponds to the real and imaginary parts of optical dielectric function of the sample. A lock-in amplifier is used to obtain second-harmonic spectral information which helps to eliminates any background far field signal. A gold mirror is used as the reference. The ferroelastic domain walls in $Sr_3Sn_2O_7$ are very well established at room temperature, allowing for line scans to be performed over a frequency range of 330 - 750 $cm^{-1}$. Each line scan consists of a series of points collected in a stepwise manner. We employ a 20 nm step size, and the spectrum at each point averages 20 separate scans. We imaged multiple different walls, although for simplicity, we show representative images here. As part of our analysis, we carried out both fixed-frequency and fixed-position cuts of the full data set. Averaging was employed as appropriate to improve the signal-to-noise ratio.

Figure 2 displays the near field infrared response of $Sr_3Sn_2O_7$ at 300 K along with the far field infrared absorption, the Raman scattering response, and the theoretically-predicted infrared-active modes for this system. This comparison makes the assignment of the near field features and their corresponding mode symmetries and displacement patterns straightforward.[17] The

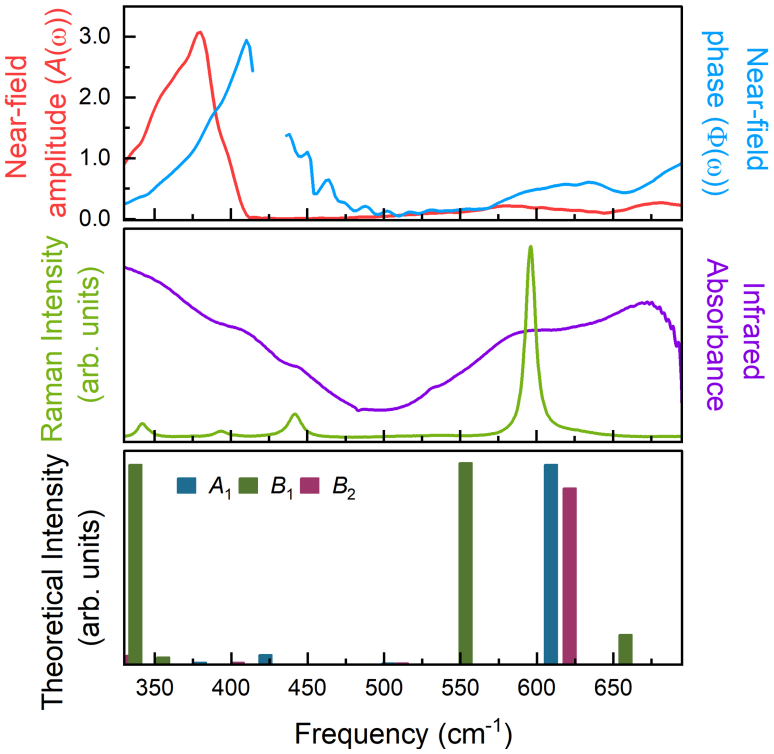


Figure 2: The synchrotron-based near field infrared amplitude (red) and phase (blue) responses are compared to the far field infrared (purple) and Raman scattering (green) spectra for $Sr_3Sn_2O_7$. The bottom panel shows the theoretically predicted phonon frequencies and their intensities,[17] color-coded based on mode assignment. Two additional theoretically-predicted $B_{2u}$ symmetry modes just below 330 cm$^{-1}$ contribute as well.[17]

traditional and near field infrared responses appear somewhat different, which is primarily a consequence of the far field vs. tip-based approach.[30] Our analysis concentrates primarily on the peak in the near field amplitude response near 380 cm$^{-1}$ which is sharp and strong. This peak is comprised of both $B_1$ and $B_2$ symmetry modes.[17] The displacement patterns correspond to various Sn-O-Sn bending motions. The Sn-O stretches near 580 and 680 cm$^{-1}$ also appear in the near field infrared data but are noticeably weaker. These peaks are also comprised of multiple modes.[17] The near field response has both amplitude $A(\omega)$ and phase $\Phi(\omega)$, corresponding to the real and imaginary parts of the signal. The amplitude corresponds most closely to reflectance or $\epsilon_1(\omega)$) whereas the phase is more akin to absorbance.[30,35] As the amplitude approaches zero, the phase is not well-defined, which explains the break in the phase spectrum. Consequently, we focus our discussion on the near field amplitude and

how it changes across a ferroelastic domain wall.

Various line scans were performed across the sample surface, and all show a consistent domain wall response. Figure 3 shows a representative ferroelastic domain wall which illustrates the typical near field response. Additional spectra and further analyses can be found in the Supporting Information. The contour plots in Fig. 3(a, b) highlight the three distinct peaks present in the frequency range of interest. Two contour plots were used due to the large amplitude intensity difference between the feature located at 380 $cm^{-1}$ and those at 580 and 676 $cm^{-1}$. The distance corresponds to the distance travelled along a designated line scan. There is a marked decrease in the scattering amplitude beginning at 440 nm

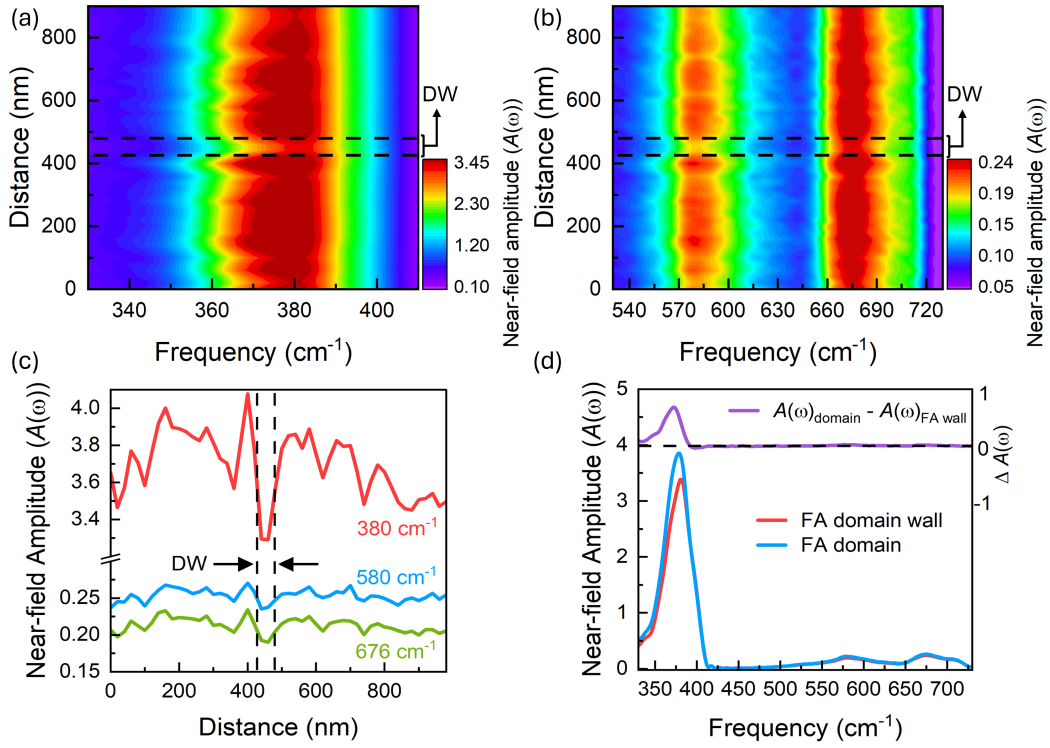


Figure 3: (a, b) Contour plots of the distance scanned versus frequency where the near field amplitude is represented by a color scale. The dotted lines indicate the location of the ferroelastic domain wall. Note the contour plot is separated into two frequency ranges due to the large amplitude differences. (c) Fixed frequency cuts are taken at each of the three distinct phonons visualized in (a) and (b). The location of the domain wall is denoted by a dotted line. There is a large dip in near field amplitude as the domain wall is crossed. (d) Fixed distance cuts are averaged over the width of the domain wall (red) and over a corresponding width in the adjacent domain (blue). The difference spectrum is plotted for clarity in purple.

which corresponds to the onset of the ferroelastic domain wall. The location of the domain wall can be further visualized in the fixed frequency plot [Fig. 3(c)], where the near field amplitude is plotted against the distance along the line scan. The amplitude decreases to a local minimum and is present in each phonon with the clearest indication being the large dip observed in the lowest frequency feature. This amplitude change can also be seen in the fixed distance cut plot in Fig. 3(d) where the amplitude response as a function of frequency from within the domain is compared to the response at the wall. The difference spectrum shows that the phonon at 380 $cm^{-1}$ has the greatest sensitivity to the presence of the wall. As a reminder, the feature near 380 $cm^{-1}$ consists of $B_1$ and $B_2$ symmetry bending modes.[17] This differs from our previous study of $Ca_3Ti_2O_7$ where the stretching modes were considerably more sensitive to the domain wall.

We can extract several important results from these data. First, the ferroelastic domain walls in $Sr_3Sn_2O_7$ are noticeably thinner than those in $Ca_3Ti_2O_7$. The domain wall shown in Fig. 3(c) is representative of the more than 20 walls imaged and is approximately 40 nm in width which is average for this material. Additional line scan data (for both thinner and thicker domain walls) are shown in the Supporting Information. At the same time, the infrared spectrum provides a sensitive and microscopic indicator of the presence (or absence) of metallic character.[34] The lack of a Drude response and the clear presence of unscreened phonons in the available frequency range clearly confirm that the wall is not metallic in nature. There are slight blue shifts of the phonon modes at the wall that are near the limit of our sensitivity. These frequency shifts are consistent with a slight hardening of the force constant - on the order of 1%.

Given the many similarities between the synchrotron near field infrared response of ferroelastic domain walls in $Sr_3Sn_2O_7$ and $Ca_3Ti_2O_7$, it's important to discuss the primary difference - which is that walls in $Sr_3Sn_2O_7$ are significantly narrower than those in $Ca_3Ti_2O_7$ [Fig. 1(e)]. There is certainly some variation in the domain wall widths in both materials. Even so, we find that twin boundary interfaces in $Sr_3Sn_2O_7$ range from approximately

20 to 60 nm whereas those in $Ca_3Ti_2O_7$ display widths between 60 and 160 nm.[25] As we discuss below, the lattice is overall softer and more flexible in $Sr_3Sn_2O_7$. This likely allows the octahedral tilt and rotational order parameters to evolve more quickly, still traversing their full range but over a shorter distance. A more relaxed lattice therefore supports strain management.

Table 1: Comparison of the experimental structural parameters in $Ca_3Ti_2O_7$ and $Sr_3Sn_2O_7$ at room temperature. The theoretical octahedral distortion amplitudes have been included for completeness. Calculated values are rounded for ease of comparison. Data taken from Refs.[9,16,25]

| **Unit cell parameters** | **$Ca_3Ti_2O_7$** | **$Sr_3Sn_2O_7$** |
|---|---|---|
| *a, b, c* (Å) | 5.42340, 5.41720, 19.41690 | 5.73330, 5.70570, 20.66370 |
| $V$ (Å$^3$) | 570.46 | 675.96 |
| $a/b$ | 1.001 | 1.005 |
| $c/a$ | 3.580 | 3.604 |
| **Bond lengths** | | |
| Equatorial Ti-O/Sn-O (Å) | 1.956(5), 1.960(4), 1.944(5), 1.950(4) | 2.0423(5), 1.9975(5), 2.0670(5), 2.0777(4) |
| Axial Ti-O/Sn-O (Å) | 1.93(3), 1.950(4) | 2.0862(8), 2.0425(0) |
| **Octahedral distortions** | | |
| $\chi_2^+$ (Å) | 1.26 | 1.09 |
| $\chi_3^-$ (Å) | 1.76 | 1.66 |
| $\tau_5^-$ (Å) | 0.89 | 0.64 |

It turns out that a simple structure-property analysis is able to account for differences in domain wall width. For instance, even though the $a/b$ and $c/a$ ratios are very similar, comparison reveals that the lattice parameters are approximately 6% larger in $Sr_3Sn_2O_7$ [Table 1]. This difference naturally translates into a larger unit cell volume. The tolerance factor is also an excellent descriptor for a wide variety of properties in this family of materials.[11,17,18] The tolerance factor of $Sr_3Sn_2O_7$ is 0.957 whereas that in $Ca_3Ti_2O_7$ is 0.946,[17] so we find that materials with larger tolerance factors have narrower walls. From a structural viewpoint, this makes sense because materials with smaller tolerance factors have larger octahedral rotation amplitudes. Phase transitions in the $n$=2 Ruddlesden-Popper materials involve changes to the octahedral rotations, and it takes more energy to drive the transition

in low tolerance factor compounds. Analysis of the local structure around the Sn center is even more convincing when tested against our near field infrared images, particularly the behavior of the Sn-O-Sn bending modes across the walls.[9] As shown in Table 1, the bonding environment around Sn is highly asymmetric, and the Sn-O bond lengths are overall longer and more distinct than the corresponding Ti-O distances.[9,25] By comparison, $Ca_3Ti_2O_7$ is a significantly stiffer material with a more symmetric coordination environment. The high temperature structural stability of $Sr_3Sn_2O_7$ is also consistent with a softer lattice.[10,17,36] These factors mandate a slower evolution of the order parameters and give rise to wider walls in $Ca_3Ti_2O_7$.

Hybrid improper ferroelectrics host an extensive network of ferroelectric and ferroelastic domain walls. As part of our program to unravel the properties of ferroelastic walls in these materials, we imaged the near field infrared response of $Sr_3Sn_2O_7$. Constant distance slices of the line scan data highlight reduced near field amplitude as well as semiconducting character at the wall. Fixed frequency cuts of the near field contour plot demonstrate the singular importance of the Sn-O-Sn bends in this system and, at the same time, point toward domain wall widths on the order of 40 nm. The latter is quite different from the situation in $Ca_3Ti_2O_7$ where both Ti-O stretching and Ti-O-Ti bending modes are active across the wall and the ferroelastic domain walls are significantly wider. We analyze the lattice constants, tolerance factors, and local structures and find that these simple descriptors are very effective tools for the development of structure-property relations. We argue that a softer lattice as in $Sr_3Sn_2O_7$ relaxes strain and supports narrower ferroelastic domain walls whereas a stiffer lattice (as in $Ca_3Ti_2O_7$) leads to wider domain walls due to the slower evolution of the order parameters. These ideas may be useful for anticipating the properties of ferroelastic domain walls in other hybrid improper ferroelectrics.

Research at the University of Tennessee is supported by Solid State and Materials Chemistry, Division of Materials Research, National Science Foundation (DMR-2129904). The work at Rutgers is supported by the W. M. Keck foundation grant to the Keck Center for Quantum Magnetism at Rutgers University. The Advanced Light Source is supported by the Office of Basic Energy Sciences, Division of Materials Sciences and Engineering, of the U.S. Department of Energy under Contract DE-AC02-05CH11231.

Standard synchrotron radiation safety protocols should be followed carefully.

Statistical information regarding the domain wall size distribution observed in $Sr_3Sn_2O_7$ can be found in the supporting information. Two additional near-field infrared spectroscopy measurements representing the maximum and minimum domain wall widths have also been included.

# References

(1) Bousquet, E., Dawber, M., Stucki, N., Lichtensteiger, C., Hermet, P., Gariglio, S., Triscone, J.-M., and Ghosez, P., Improper ferroelectricity in perovskite oxide artificial superlattices, Nature, (2008) **452**, 732-736. DOI: https://doi.org/10.1038/nature06817

(2) Benedek, N. A. and Fennie, C. J., Hybrid improper ferroelectricity: a mechanism for controllable polarization-magnetization coupling, Phys. Rev. Lett. (2011) **106**, 107204. DOI: 10.1103/PhysRevLett.106.107204.

(3) Harris, A. B., Symmetry analysis for the Ruddlesden-Popper systems $Ca_3Mn_2O_7$ and $Ca_3Ti_2O_7$, Phys. Rev. B (2011) **84**, 064116. DOI: 10.1103/PhysRevB.84.064116.

(4) Benedek, N. A. and Fennie, C. J., Polar octahedral rotations: a path to new multifunctional electronic, magnetic, and orbital materials, J. Solid State Chem. (2012) **195**, 11-20. DOI: 10.1016/j.jssc.2012.04.012.

(5) Benedek, N. A. and Fennie, C. J., Why are there so few perovskite ferroelectrics?, J. Phys. Chem. (2013) **117**, 13339-13349. DOI: https://doi.org/10.1021/jp402046t

(6) Oh, Y. S., Luo, X., Huang, F.-T., Wang, Y., and Cheong, S.-W., Experimental demonstration of hybrid improper ferroelectricity and the presence of abundant charged walls in $(Ca,Sr)_3Ti_2O_7$ crystals, Nat. Mater. (2015) **14**, 407. DOI: 10.1038/nmat4168.

(7) Benedek, N. A., Rondinelli, J. M., Djani, H., Ghosez, P., and Lightfoot, P., Understanding ferroelectricity in layered perovkites: new ideas and insights from theory and experiments, Dalton Trans. (2015) **44**, 10544-10558. DOI: 10.1039/C5DT00010F.

(8) Nowadnick, E. A. and Fennie, C. J., Domains and ferroelectric switching pathways in $Ca_3Ti_2O_7$ from first principles, Phys. Rev. B. (2016) **94**, 104105. DOI: https://doi.org/10.1103/PhysRevB.94.104105

(9) Wang, Y., Huang, F. -T., Luo, X., Gao, B., and Cheong, S. -W., The first room-temperature ferroelectric Sn insulator and its polarization switching kinetics, Adv. Mater. (2017) **29**, 1601288. DOI: https://doi.org/10.1002/adma.201601288

(10) Yoshida, S., Fujita, K., Akamatsu, H., Hernandez, O., Gupta, A. S., Brown, F. G., Padmanabhan, H., Gibbs, A. S., Kuge, T., Tsuji, R., Murai, S., Rondinelli, J. M., Gopalan, V., and Tanaka, K., Ferroelectric $Sr_3Zr_2O_7$: competition between hybrid improper ferroelectric and antiferroelectric mechanisms, Adv. Funct. Mater. (2018) **8**, 1801856. DOI: https://doi.org/10.1002/adfm.201801856

(11) Yoshida, S., Akamatsu, H., Tsuji, R., Hernandez, O., Padmanabhan, H., Gupta, A. S., Gibbs, A. S., Mibu, K., Murai, S., Rondinelli, J. M., Gopalan, V., Tanaka, K., and Fujita, K., Hybrid improper ferroelectricity in $(Sr,Ca)_3Sn_2O_7$ and beyond: universal relationship between ferroelectric transition temperature and tolerance factor in $n$ = 2 Ruddlesden-Popper phases, J. Am. Chem. Soc. (2018) **140**, 15690-15700. DOI: https://doi.org/10.1021/jacs.8b07998

(12) Ye, F., Wang, J., Sheng, J., Hoffmann, C., Gu, T., Xiang, H. J., Tian, W., Molaison, J. J., dos Santos, A. M., Matsuda, M., Chakoumakos, B. C., Fernandez-Baca, J. A., Tong, X., Gao, B., Kim, J. W., and Cheong, S. -W., Soft antiphase tilt of oxygen octahedra in the hybrid improper multiferroic $Ca_3Mn_{1.9}Ti_{0.1}O_7$, Phys. Rev. B (2018) **97**, 041112(R). DOI: https://doi.org/10.1103/PhysRevB.97.041112

(13) Xu, X., Wang, Y., Huang, F. -T., Du, K., and Cheong, S. -W., Highly tunable ferroelectricity in hybrid improper ferroelectric $Sr_3Sn_2O_7$. Adv. Funct. Mater. (2020) **30**, 2003623. DOI: 10.1002/adfm.202003623

(14) Cherian, J. G., Birol, T., Harms, N. C., Gao, B., Cheong, S. -W., Vanderbilt, D., and Musfeldt, J. L., Optical spectroscopy and band gap analysis of hybrid improper ferroelectric $Ca_3Ti_2O_7$, Appl. Phys. Lett. (2016) **108**, 262901. DOI: https://doi.org/10.1063/1.4954404

(15) Wang, B., Lin, H., Xu, J., Chen, H., Lin, Z., Huang, F., and Wang, Y., Design, preparation, and characterization of a novel red long-persistent perovskite phosphor: $Ca_3Ti_2O_7:Pr^{3+}$, Inorg. Chem. (2015) **54**, 11299-11306. DOI: https://doi.org/10.1021/acs.inorgchem.5b01894

(16) Ramkumar, S. P. and Nowadnick, E. A., Octahedral rotations in Ruddlesden-Popper layered oxides under pressure from first principles, Physical Review B (2021) **104**, 144105. DOI: https://doi.org/10.1103/PhysRevB.104.144105

(17) Smith, K. A., Ramkumar, S. P., Harms, N. C., Clune, A. J., Xu, X., Cheong, S. -W., Liu, Z., Nowadnick, E. A., Musfeldt, J. L., Revealing pressure-driven structural transitions in hybrid improper ferroelectric $Sr_3Sn_2O_7$, Physical Review B (2021) **104**, 064105. DOI: https://doi.org/10.1103/PhysRevB.104.064106

(18) Geisler, B., Hamlin, J. J., Stewart, G. R., Hennig, R. G., and Hirschfeld, P. J., Structural transitions, octahedral rotations, and electronic properties of $A_3Ni_2O_7$ rare-earth nickelates under high pressure, npj Quantum Materials (2024) **9**, 38. DOI: https://doi.org/10.1038/s41535-024-00648-0

(19) Senn, M. S., Bombardi, A., Murray, C. A., Vecchini, C., Scherilo, A., Luo, X., and Cheong, S. -W., Negative thermal expansion in hybrid improper ferroelectric Ruddlesden-Popper perovskites by symmetry trapping, Phys. Rev. Lett. (2015) **114**, 035701. DOI: 10.1103/PhysRevLett.114.035701.

(20) Senn, M. S., Murray, C. A., Luo, X., Wang, L., Huan, F. -T., Cheong, S. -W., Bombardi, A., Ablitt, C., Mostofi, A. A., and Bristowe, N. C., Symmetry switching of negative thermal expansion by chemical control, J. Am. Chem. Soc. (2016) **138**, 5479-5482. DOI: 10.1021/jacs.5b13192.

(21) Huang, L. -F., Lu, X. -Z., and Rondinelli, J. M., Tunable negative thermal expansion in layered perovskites from quasi-two-dimensional vibrations, Phys. Rev. Lett. (2016) **117**, 115901. DOI: https://doi.org/10.1103/PhysRevLett.117.115901

(22) Evans, D. M., Garcia, V., Meier, D., and Bibes, M., Domains and domain walls in multiferroics, Physical Science Reviews (2020) 20190067. DOI: https://doi.org/10.1515/psr-2019-0067

(23) Huang, F. -T., Xue, F., Gao, B., Wang, L. H., Luo, X., Cai, W., Lu, X. -Z., Rondinelli, J. M., Chen, L. Q., and Cheong, S. -W., Domain topology and domain switching

kinetics in a hybrid improper ferroelectric, Nature Comm. (2016) **7**, 11602. DOI: 10.1038/ncomms11602.

(24) Lee, M. -H., Chang, C. -P., Huang, F. T., Guo, G. Y., Gao, B., Chen, C. H., Cheong, S. -W., and Chu, M. -W., Hidden antipolar order parameter and entangled Néel-type charged domain walls in hybrid improper ferroelectrics, Phys. Rev. Lett. (2017) **119**, 157601. DOI: 10.1103/PhysRevLett.119.157601.

(25) Smith, K. A., Nowadnick, E. A., Fan, S., Khatib, O., Lim, S. J., Gao, B., Harms, N. C., Neal, S. N., Kirkland, J. K., Martin, M. C., Won, C. J., Raschke, M. B., Cheong, S. W., Fennie, C. J., Carr, G. L., Bechtel, H. A., and Musfeldt, J. L., Infrared nanospectroscopy of ferroelastic domain walls in hybrid improper ferroelectric $Ca_3Ti_2O_7$, Nat. Commun. (2019) **10**, 1. DOI: https://doi.org/10.1038/s41467-019-13066-9

(26) Kumagai, Y. and Spaldin, N. A., Structural domain walls in polar hexagonal manganites, Nat. Commun. (2013) **4**, 1540. DOI: https://doi.org/10.1038/ncomms2545

(27) Moreno, R., Evans, R. F. L., Khmelevskyi, S., Muñoz, M. C., Chantrell, R. W., and Chubykalo-Fesenko, O., Temperature dependent exchange stiffness and domain wall width in Co, Phys. Rev. B (2016) **94**, 104433. DOI: https://doi.org/10.1103/PhysRevB.94.104433

(28) Catalan, G., Seidel, J., Ramesh, R., Scott, J. F., Domain wall nanoelectronics, Rev. Mod. Phys. (2012) **84**, 119. DOI: https://doi.org/10.1103/RevModPhys.84.119

(29) Carr, G. L., Resolution limits for infrared microspectroscopy explored with synchrotron radiation, Rev. Sci. Inst. (2001) **72**, 1613-1619. DOI: https://doi.org/10.1063/1.1347965

(30) Bechtel, H. A., Muller, E. A., Olmon, R. L., Martin, M. C., and Raschke, M. B., Ultrabroadband infrared nanospectroscopic imaging, Proc. Natl. Acad. Sci. (2014) **111**, 7191-7196. DOI: https://doi.org/10.1073/pnas.1400502111

(31) Muller, E. A., Pollard, B., and Raschke, M. B., Infrared chemical nanoimaging: accessing structure, coupling, and dynamics on molecular length scales, J. Phys. Chem. Lett. (2015) **6**, 1275-1284. DOI: https://doi.org/10.1021/acs.jpclett.5b00108

(32) Khatib, O., Bechtel, H. A., Martin, M. C., Raschke, M. B., and Carr, G. L., Far infrared synchrotron near-field nanoimaging and nanospectroscopy, ACS Photonics (2018) **5**, 2773-2779. DOI: https://doi.org/10.1021/acsphotonics.8b00565

(33) Mastel, S., Govyadinov, A. A., Maissen, C., Chuvilin, A., Berger, A., and Hillenbrand, R., Understanding the image contrast of material boundaries in IR nanoscopy reaching 5 nm spatial resolution, ACS Photonics, (2018) **5** 3372-3378. DOI: https://doi.org/10.1021/acsphotonics.8b00636

(34) Bechtel, H. A., Johnson, S. C., Khatib, O., Muller, E. A., and Raschke, M. B., Synchrotron infrared nano-spectroscopy and imaging, Surface Science Reports (2020) **75**, 100493. DOI: https://doi.org/10.1016/j.surfrep.2020.100493

(35) Govyadinov, A. A., Amenabar, I., Huth, F., Carney, P. S., and Hillenbrand, R., Quantitative measurements of local infrared absorption and dielectric function with tip-enhanced near-field microscopy, J. Phys. Chem. Lett. (2013) **4**, 1526-1531. DOI: https://doi.org/10.1021/jz400453r

(36) Kratochvilova, M., Huang, F. T., Diaz, M. T. F., Klicpera, M. Day, S. J. Thompson, S. P., Oh, Y. S., Gao, B. Cheong, S. W., and Park, J. G., Mapping the structural transitions controlled by the trilinear coupling in $Ca_{3-x}Sr_xTi_2O_7$, J. Appl. Phys. (2019) **125**, 244102. DOI: https://doi.org/10.1063/1.5089723

# TOC Graphic

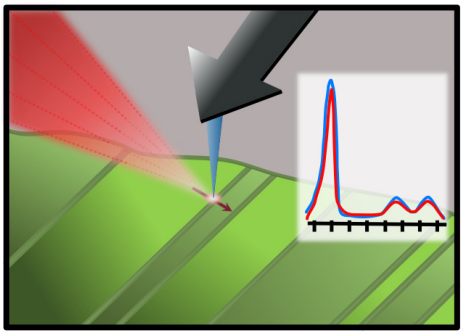

For Table of Contents Only